Applied Thermal Engineering 230 (2023) 120685

Contents lists available at ScienceDirect

Applied Thermal Engineering

journal homepage: www.elsevier.com/locate/apthermeng

Research Paper

Analysis of the aging effects on the thermal runaway characteristics of Lithium-Ion cells through stepwise reactions

José Vicente Pastor, Antonio García *, Javier Monsalve-Serrano, Diego Golke

CMT - Motores Térmicos, Universitat Politècnica de València, Camino de Vera s/n, 46022 Valencia, Spain

ARTICLE INFO

Keywords:
Battery Thermal Runaway
Chemical Kinetics
Aging
Electrochemical Model
Step-Wise reactions
Vehicle Safety

ABSTRACT

The current political vision to drastically reduce carbon emissions pushes the electrified powertrain into an increasingly important role in the transport sector. However, concerns related to the battery's effectiveness as an energy source need to be overcome to make this technology widespread. One such concern is safety, catching attention as development races towards greater battery energy density. In this way, cathodic chemistry is important since exothermic reactions are unleashed from the components that originally formed the active material. Furthermore, the aging process reduces the battery capacity, reducing the amount of active material and thickening the solid electrolyte interface, which increases the joule effect. For these reasons, thermal runaway under aging conditions must be investigated to assess potential safety issues. Using an accelerating rate colorimeter, the heat-induced thermal runaway tests were performed with two-cathode chemistry (NMC and LFP) under pristine and aged battery conditions. For aging the batteries, the ARC was coupled with a bidirectional source. Two ambient temperatures, 20 °C and 50 °C, were used for the aging tests, being the batteries cycled up to 250 cycles with a determined protocol for charge and discharge. A numerical model was fed with experimental tests, targeting optimizing the battery output parameters and obtaining geometric aspects that are difficult to measure. Unlike the single step model, a stepwise reactions model was created to assess the heat release from different battery components for pristine and aged conditions. The higher endothermic behavior from cathode decomposition and less oxygen released during this reaction make the LFP battery safer than the NMC. For aged batteries, the SEI growth consumes lithium and electrolyte, decreasing the quantity of both components in the anode. Thus, the anode and electrolyte reaction after SEI decomposition is lower, improving battery safety.

1. Introduction

Electric vehicles (EVs) are the leading solution for achieving the requirements of zero tailpipe CO_2 emissions in 2050, as stipulated by the European parliament. Based on that, governments and manufacturers are pushing the electric vehicle development to turn this technology reliable and widespread. However, the major bottleneck is the battery as the energy storage system for EVs [1]. The main concerns arise from recharge time, energy density, raw materials supply and durability. In addition, the requirement of greater vehicle range autonomy makes the battery packaging more complex, resulting in a complicated cooling system that can decrease cooling effectiveness [2]. For those reasons, thermal issues due to increased demand on energy density and ineffective cooling can lead to thermal runaway, resulting in significant safety concerns that need to be studied. Furthermore, the batteries suffer from cycling, reducing capacity and performance [3]. These losses are related to active material, electrolyte substance, and solid electrolyte interface that directly impact the chain reaction of thermal runaway phenomena [4,5].

This chain reaction occurs step by step, releasing heat in such a way that it can be self-sustaining, becoming unstoppable. The first heat released is attributed to the solid electrolyte interface (SEI)

Abbreviations: ARC, Accelerating rate calorimeter; CCCV, Constant-current constant-voltage; CO_2, Carbon dioxide; DFN, Doyle-Fuller-Newman; DSC, Differential Scanning Calorimetry; EVs, Electric vehicles; LMO, Lithium manganese oxide; LFP, Lithium iron phosphate battery; NMC, Lithium Nickel Cobalt Manganese Oxide; ODEs, Ordinary differential equations; P2D, Pseudo-two-dimensional; SEI, Solid electrolyte interface; SOC, State of charge; TR, Thermal runaway; WLTC, Worldwide Harmonised Light Vehicles Test Procedure; XRD, X-ray diffraction analysis.

* Corresponding author.
E-mail address: angarma8@mot.upv.es (A. García).

https://doi.org/10.1016/j.applthermaleng.2023.120685
Received 20 December 2022; Received in revised form 15 March 2023; Accepted 30 April 2023
Available online 5 May 2023

decomposition, which generally occurs at about 100 °C [6]. At this moment, the SEI starts to decompose and regenerate, constantly releasing heat and increasing the battery's internal temperature. This stage is known as stage I heat production. In sequence, the separator, normally manufactured with polypropylene or polyethylene, is melted when the battery temperature achieves 120–130 °C. A short circuit occurs due to the inexistence of protection between the anode and cathode, producing more heat according to Joule's law. This phase is called stage II heat spread. The solvent from the electrolyte starts to decompose in hydrogen and hydroxide radicals, which can trigger the electrolyte's combustion process [7]. In addition, the cathode material decomposes, releasing the oxygen that will supply the combustion process. During the sequence of events, the temperature and internal pressure due to the gas generated increase. When the internal pressure exceeds a determined value, the venting cap bursts, releasing the gases, avoiding case rupture and disasters [8].

The above events can change according to the battery chemistry [9]. For example, Li et al. [10] performed experimental tests of battery thermal abuse using an accelerating rate calorimeter (ARC) with different battery cathode chemistries. The results showed a similar onset temperature of about 90 °C. However, the batteries' maximum temperature, maximum temperature rise rate and the heat of reaction were different. The lithium nickel cobalt manganese oxide (NMC) has presented the highest values for the mentioned parameters, followed by the lithium manganese oxide (LMO) and lithium iron phosphate battery (LFP). Furthermore, other parameters, such as the state of charge and thermal runaway trigger (short circuit, external heating, etc.) can also influence and change the chain reaction and thermal runaway characteristics [11].

Another crucial point that, however, is less addressed in thermal runaway studies is that most of the work uses new batteries, because even if fresh cells show acceptable safety behavior, this may change upon aging. Waldmann and Mehrens [12] have investigated the aging effect at 0 °C in order to increase the lithium plating phenomenon and assess the safety issues using an ARC. The results showed that in addition to increasing capacity loss, battery aging showed an earlier thermal runaway event and more drastic decomposition, injecting the jelly roll from the cell can. The aging effect on thermal runaway is not straightforward. For a while, some authors observed a decrease in certain safety properties. In contrast, others have found improvements [13]. However, it is well-known that aging mechanisms change the properties of the materials inside Li-ion cells [14].

Modeling is key for understanding the different processes during the thermal runaway phenomenon. A simplified way is called single step thermal runaway model [15]. It assumes that the thermal runaway occurs as a sudden and irreversible process once a certain temperature threshold is reached [16]. This model is based on the observation that once a battery begins to heat up due to an internal failure, the heat generated can accelerate the reaction, leading to an exponential rise in temperature [17]. While the single-step model is relatively simple and computationally efficient [18], it may not capture the complex thermal and electrochemical processes that occur in real batteries, and its accuracy may depend on the specific criterion used [19]. To overcome this problem, this paper proposes coupling a pseudo-two-dimensional (P2D) model with stepwise reactions to qualitatively quantify and understand where the heat source during the thermal runaway is, which experimentally is measured as just a final global value of heat release [20–22]. The P2D is a popular choice for battery design because it offers several advantages over other battery models [23]. Firstly, the P2D model is more accurate than simpler models such as the equivalent circuit model. This is because it considers the spatial distribution of active materials within the electrodes, which can affect the battery's performance [24]. Secondly, the P2D model is more computationally efficient than three-dimensional models, making it a more practical choice for large-scale simulations. Finally, the P2D model can provide insights into the internal dynamics of the battery, such as the formation and evolution of lithium dendrites, which are difficult to observe experimentally [25]. Overall, the P2D model balances accuracy and computational efficiency well, making it a powerful tool for battery design and optimization. Stepwise reactions can be coupled to the P2D model, getting the results of battery design optimization and feeding the main reaction that takes place inside the battery that leads to thermal runaway. Few works have explored the potential of stepwise reactions, generally using standard values to compare different design of batteries [26]. Most of the work available on the topic is focused on developing the stepwise reactions, comparing the results with measurements made mainly in differential scanning calorimetry (DSC) [27–29].

This work investigates the aging effect on the battery thermal runaway (TR) phenomenon for two different cathode chemistry, NMC and LFP. To achieve this goal, an ARC was coupled with an Arbin bidirectional source in order to cycle the batteries at two different temperatures, 20 and 50 °C. First, performance tests were carried out with pristine batteries at both ambient temperatures. The aging process was carried out up to 250 cycles, using a charging protocol up to maximum voltage, rest and discharge at 2C-rate. In sequence, the aged batteries were tested in an ARC to evaluate the thermal runaway behavior using the heat-wait-seek protocol. Pristine batteries were also tested with the same protocol used for the aged batteries, targeting a comparison. Performance and aging results were also used to create and calibrate a P2D battery cell model using GT-Autolion software and evaluate information about geometric aspects of the battery that are difficult to measure. These results were used to feed a heat release calculator with stepwise reactions, representing the most representative reactions during the heat release process. Therefore, the stepwise reactions were used to give insight into the aging effect on TR and support the experimental results.

2. Methods

To ensure the robustness of the methodology, as well as to observe the differences between different battery chemistries, two different cathode compositions were included in this evaluation with different degradation conditions and the tested conditions were performed three times each. For the NMC cathode, the Samsung INR18650-20R was selected, while the NX 9073 was considered for the LFP chemistry. In both cases, the anode is composed of graphite. A summary of their properties is included in Table 1. From the properties reported, it can be seen that the NMC (Nickel-Manganese-Cobalt, LiNiMnCoO2) provides better performance in terms of total capacity and peak performance with a specific energy density that reaches 169 Wh/kg, while the LFP (Lithium Iron Phosphate, LiFePO4) remains at a maximum of 139 Wh/kg with current levels and peak voltages much lower.

2.1. Experimental setup

For the experimental characterization and evaluation of the cells,

Table 1
Main Lithium-Ion cell properties for the NMC and LFP cathodes.

Parameter	NMC	LFP
Cell format	18,650	18,650
Cathode Chemistry	$LiNiMnCoO_2$	$LiFePO_4$
Dimensions [mm]	18.3 × 65.0	18.2 × 65.2
Weight [g]	42.4	41.5
Nominal Voltage [V]	3.6	3.2
Nominal Capacity [Ah]	2.0	1.8
Current Charge Continuous/Peak [A]	2.0/4.0	1.8/-
Current Discharge Continuous/Peak [A]	22.0/30.0A	5.4/10
Total Energy [Wh]	7.2	5.8
Vent Cap holes	3	3
Voltage at 100% SOC [V]	4.2	3.65
Cut-off voltage [V]	2.5	2.5
Temperature use Range [°C]	−20 to 60	−20 to 50

two different equipment have been employed in this work to control both electrical and thermal working conditions of the cells during the electrical characterization, the aging process and final thermal abuse tests.

The electrical demand on the cells was controlled by a bidirectional power source LBT-10 V-100A from Arbin Instruments [30]. This high-accuracy battery cycler can provide voltages ranging from 0 to 10 V with an accuracy of ± 4 mV, and current from 500 mA up to 100A with a control accuracy of ± 0.04% of the range used. By programming the charging/discharging profiles, different types of tests are applied to the cell. The most relevant protocols for this study are constant current discharge for performance characterization and battery cycling, constant-current constant-voltage (CCCV protocol) for charging process and state of charge (SOC) definition, and different transient profiles defined for electric vehicle applications that were used to feed detailed electrochemical models as explained in 2.4 Modelling framework.

For controlling the thermal state of the working ambient of the cell, an accelerating rate calorimeter (ARC) from Thermal Hazards Technologies was used [31]. This device provided an enclosed environment where a constant ambient temperature can be maintained while performing the electrical tests with an accuracy over ambient temperature of ± 0.2%. This constant temperature mode was applied for both, battery performance characterization and cycling, which provided data on the different impacts that this could have on battery capacity degradation for both chemistries. Apart from this application, the original purpose of the ARC is to carry out destructive tests of thermal abuse on the cells to evaluate battery thermal runaway. The control used for the wall temperatures allows the heat-wait-seek method to achieve an almost adiabatic process in which the battery is warmed up until the exothermic process from the battery thermal runaway overcomes the external heating [32]. According to manufacturing, the ARC is equipped with N-type thermocouples with 0.001 °C resolution and an accuracy of 0.7%. The exothermic mode was activated when the battery temperature rise rate was higher than 0.02 °C/min during seek period. This high sensitivity is obtained by performing a calibration procedure before the experimental tests, where the calorimeter system calibrates the output voltage of the thermocouples in the test temperature range with half sensitivity used during the experimental tests. This ensures that there are no battery temperature drift issues, being any temperature rise rate greater than 0.02 °C/min a result of an exothermic reaction. This thermal abuse test was applied on both pristine and aged cells. A summary of the uncertainties related to measurements is shown in Table 2.

Additionally, throughout the electrical performance and aging tests, type-K thermocouples were used to monitor the cell surface temperature and registered using an Agilent 34901A datalogger at a frequency of 10 Hz synchronized with the data acquisition of the Arbin battery cycler to match the data of current, voltage and temperature. A scheme of the equipment and measurement systems is presented in Fig. 1b, and Fig. 1a shows the CMT facilities used for this work.

2.2. Performance and aging tests

The electric performance tests consisted of constant-current discharge profiles at different C-rates ranging from 0.1 up to 3. Before each discharge, a CCCV charging process was applied to ensure maximum capacity and 100% SOC before each test, with a resting period of 1 h to ensure internal homogeneous lithium distribution. Transient

Table 2
Uncertainties related to measurements.

Parameter	Uncertainty
Arbin bidirectional source	± 4 mV (Voltage) ± 0.04% of the range used (Current)
N-type thermocouple	0.7%
Sensitive for exothermic reaction	0.02 °C/min

(a)

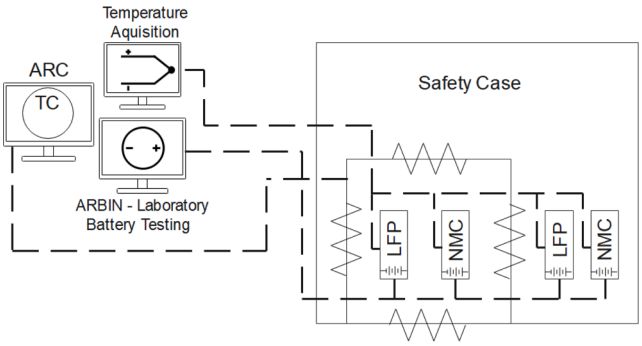

(b)

Fig. 1. Experimental Set up with the ARC EV + and current source in CMT-UPV battery lab (a) and the scheme of the batteries connection for the testing (b).

tests consisted of a programmed current demand profile representative of different driving scenarios like the Worldwide Harmonised Light Vehicles Test Procedure (WLTC) cycle. After the performance tests, the degradation tests were performed. The charge process during the cycling tests (aging tests) was different from that used in the performance and thermal runaway tests due to the long time required for battery aging. A constant current of 1C-rate was applied until reaching the maximum voltage of the cell. The battery rested for 30 min in sequence, and a discharge process occurred. For the cycling test, the discharge rate was 2C-rate to have more severe conditions and save testing time. The ambient temperature remained constant due to the ARC controller with a less than 0.2% variation. Charge and discharge cycles were carried out with a rest period of 30 min between processes. A schematic of the aging procedure is detailed in Fig. 2. The target was to achieve 250 cycles (charge-rest-discharge-rest). This protocol implies 30 days of testing without stopping. The temperature, voltage and current were recorded with a frequency of 0.1 Hz (time step of 10 s).

2.3. Thermal runway tests

The cell was fixed on a metal base to prevent movement during the test. The test was performed under constant pressure conditions. The ARC releases the increase of pressure during TR. The thermal runaway tests were performed using the heat-wait-seek mode, with a heating ramp of 5 °C and a waiting period of 30 min. If the ARC controller did not detect the exothermic reaction during seek period, the steps heat-wait-seek are repeated. The exothermic reaction mode was triggered if the battery temperature rise rate was higher than 0.02 °C/min throughout the seek period. The first step was performed at 50 °C. A scheme of the steps followed by the ARC EV + is shown in Fig. 3. Type N thermocouples were used to measure the battery temperature. One was

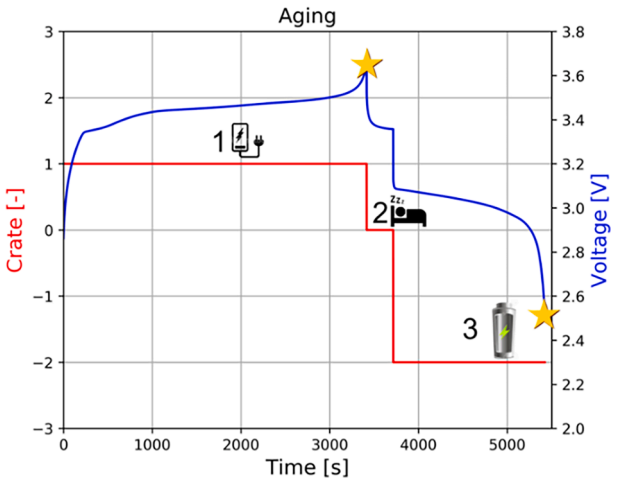

Fig. 2. Aging test protocol with charging, rest and discharge. The values are representative of a LFP cell.

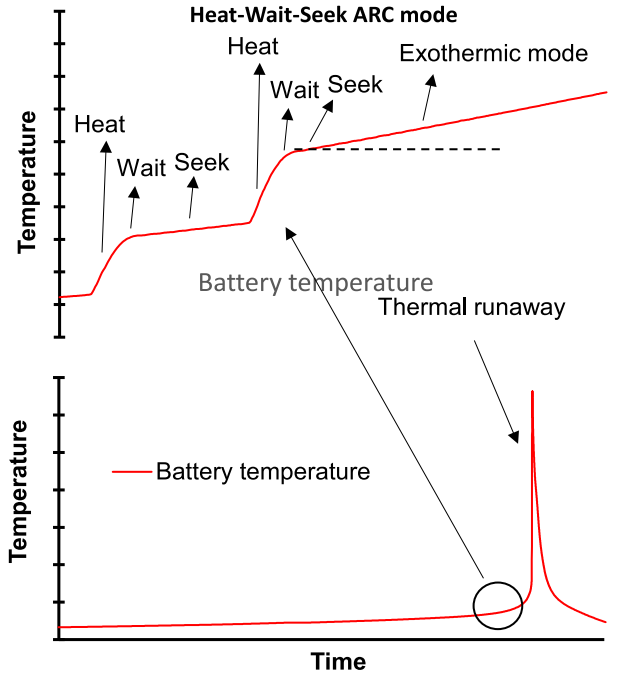

Fig. 3. Thermal runaway ARC EV + test protocol with the heat-wait-seek steps.

located in the middle of the cell to track the exothermic reaction (master thermocouple). The other thermocouple was near the venting cap to detect the venting process before the thermal runaway. Both thermocouples were glued to the battery external surface.

2.4. Modeling framework

Stepwise reactions were used to calculate the heat release from different reactions inside the battery during thermal runaway. This approach considers only a few equations, not requiring chemical kinetics to calculate component amounts. This simplification avoids high computational costs, frequently occurring when dealing with mechanisms with many equations to solve. Furthermore, the heat release calculated from the stepwise reactions not consider the binder decomposition and other side reactions less critical.

To determine specific internal parameters and how they evolve during aging, a digital twin of the cells is calibrated using the GT-AutoLion package from Gamma Technologies. In the following sections, the basics of the model as well as the calibration procedure are described. For the aging process, only solid electrolyte interface (SEI) growth was considered, because mechanisms such as lithium plating or material cracking, as well as mechano-electrochemical interaction through an active material swelling increase the number of degradation models and can be overwhelming and difficult to calibrate and discern.

2.4.1. Heat release calculator based on stepwise reactions

Sandia has developed a heat release calculator based on stepwise reactions to predict heat release from thermal runaway for most lithium-ion cathode chemistries available [26]. For the NMC chemistry, the cathode decomposition recommended to use are based on the delithiated form of the layered lithium transition metal oxide, MO_2, where M stands for Ni, Co and Mn composition. The delithiated form is relatively unstable compared to the lithiated form in the cathode. According to [33], the decomposition of MO_2 can lead to two main reaction pathways. The first can occur with oxygen release and the formation of an intermediate non-lithiated spinel M_3O_4. The other path occurs without oxygen release, forming the lithiated spinel LiM_2O_4. Combining both path reactions aforementioned, the reaction for the first part of the NMC cathode decomposition can be written as Eqn. 1

$$3x\,LiMO_2 + 2(1-x)MO_2 \rightarrow 3x\,LiM_2O_4 + (1-2x)M_3O_4 + (1-2x)O_2 \quad (1)$$

The products resulting from Reaction (1) may be converted to a thermodynamically stable molecule. The non-lithiated spinel M_3O_4 may produce rocked salt and release oxygen. Furthermore, the lithiated spinel LiM_2O_4 may also produce rocked salt, layered lithium transition metal oxide and release oxygen. Combining both reactions, the reaction can be written as Eqn. 2

$$6x\,LiM_2O_4 + 2(1-2x)M_3O_4 \rightarrow 6x\,LiMO_2 + 6(1-x)MO + (1+x)O_2 \quad (2)$$

The Reaction (1) is likely to occur as the Gibbs free energy is more negative than the global reaction for cathode decomposition [29], which is given by Eqn. 3

$$2MO_2 \rightarrow 2MO + O_2 \quad (3)$$

In addition, the presence of rocked salt is not observed during the cathode decomposition in the tests carried out with X-ray diffraction analysis (XRD) [34]. However, the presence of electrolyte can boost the reaction rate in rocked salt production via Reaction (2) and Reaction (3). Nevertheless, compared with calorimeter data, the two-step reactions (Reaction (1) and Reaction (2)) should be more adequate to model cathode decomposition for thermal runaway with a vented event, once there is evidence that the electrolyte quantity present drives the reaction rate to the Reaction (1) [33].

For electrolyte oxidation, the pressure increase favors the complete oxidation process (case before venting cap bust), while partial oxidation is preferred as the temperature increase (in the case after venting cap bust) [29]. As most of the gases vented from the battery during the thermal runaway are CO_2, a product from a complete combustion process, the full oxidation reaction is considered in the current work as Eqn. 4 to predict the heat release [35]

$$Electrolyte + O_2 \rightarrow CO_2 + H_2O \quad (4)$$

The recommended reaction for the anode and electrolyte is given by Eqn. 5 [27,28]

$$LiC_6 + electrolyte \rightarrow C_6 + C_2H_4 + Li_2CO_3 \quad (5)$$

This reaction is similar to the SEI global reaction formation [26]. The reactions described are suitable for NMC cathode chemistry. For the LFP cathode chemistry, the thermal runaway chain reaction is different, since the transition metal is more thermal stable [36]. The strong

covalent bond between $(PO_4)^{3-}$ present in FePO4, which is the delithiated form of $LiFEPO_4$, makes it to be difficult the oxygen release at high temperatures [37]. For this reason, the oxygen released during cathode heating is less than layered metal oxide cathodes, accounting for half the amount of oxygen released when both are compared [38]. The cathode decomposition suggested by Röder et al. [39] was used in the current work and it is given as Eqn. 6

$$FePO_4 \rightarrow \frac{1}{2}Fe_2P_2O_5 + \frac{1}{4}O_2 \tag{6}$$

Despite some works that have reported higher temperatures than 350 °C for the LFP cathode decomposition [40], the presence of electrolyte in contact with the cathode can act as a catalysator, decreasing the cathode temperature decomposition. This behavior was observed after ARC and Differential Scanning Calorimetry (DSC) tests [41,42].

In addition to the reactions above, the mean reaction involving the solid electrolyte interface (SEI) decomposition was also considered. The SEI is a thin layer that forms on the surface of the electrodes in a lithium-ion battery. This layer plays a crucial role in the battery's performance by controlling the flow of ions between the electrolyte and the electrodes. However, over time, the SEI layer can grow and thicken, decreasing the battery's capacity and increasing its internal resistance. This process is a major contributor to lithium-ion battery aging and is essential in heat release during thermal runaway. For this reason, the SEI decomposition is important to understand the thermal runaway process, and the main reaction is given by Eqn. 7 [43]

$$(CH_2OCO_2Li)_2 \rightarrow Li_2CO_3 + C_2H_4 + CO_2 + O_2 \tag{7}$$

The heat of reactions of the aforementioned reactions is depicted in Fig. 4, and they are in accordance with the works [26,29,44].

2.4.2. Lithium-Ion battery model

The GT-AutoLion package provides a pseudo-two-dimensional (P2D) electrochemical model for battery modelling. This P2D model was initially developed by Newman et al. [45] and it is also referred to as the Doyle-Fuller-Newman (DFN) model.

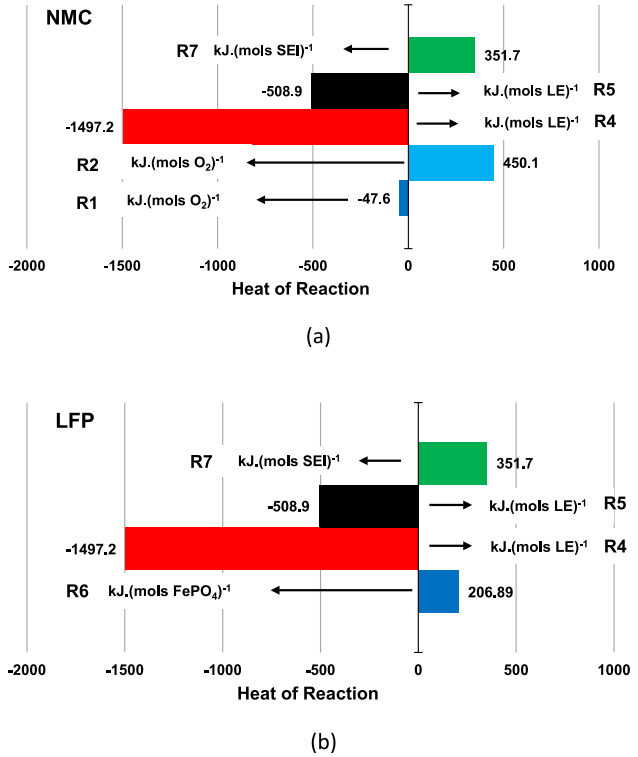

Fig. 4. Heat of reaction used in the stepwise reactions.

The model is conceptualized around the porous electrode theory, in which it is assumed that the electrode material behaves as a solid porous media formed by particles. Lithium-ion intercalation process occurs through these particles surfaces and are transmitted from one electrode to another through the electrolyte solution. A first longitudinal direction is defined from anode to cathode considering the separator in between, accounting for the macroscopic transport of species. The difference in concentration of ions will produce the potential difference in the cell. A second dimension is added through a pseudo-dimension that accounts for the radial direction inside the particles of both electrodes, in which lithium-ion radial diffusion controls the lithium intercalation process. A schematic of the model can be found in Fig. 5.

To numerically define the model, a system of ordinary differential equations is defined, accounting for mass balance, species conservation and charge conservation. Mass balance and species conservation, in particular, are governed by two equations, one in the radial direction of the particles and the other for through-plane macroscopic transport. In the macro scale, charge conservation adds two more ordinary differential equations (ODEs) for solid phase and electrolyte, respectively. This ODE system is then closed using the Butler-Volmer equation, which defines lithium intercalation reaction rates. The temperature evolution requires an additional governing equation for thermal balance, in which the thermal behavior of the cell assumes a lumped mass with different heat sources (electrochemical reactions, internal resistance, and entropic heat generation) and heat transfer boundaries (convective heat transfer to the ambient or conductive heat transfer to a cooling system for example). The general ODE system is described by Eq. (8) to Eq. (12), and more details about the specifics can be found in [1].

$$\text{Electrolyte species conservation } \frac{\partial}{\partial_x}[\varepsilon c_e] = \frac{\partial}{\partial_x}\left(D_e^{eff}\frac{\partial c_e}{\partial x}\right) + \frac{1-t_+^0}{F}j^{Li} \tag{8}$$

$$\text{Solid phase particles species conservation } \frac{\partial c_s}{\partial_x} = \frac{1}{r^2}\frac{\partial}{\partial_x}\left(D_s r^2 \frac{\partial c_s}{\partial r}\right) \tag{9}$$

$$Solidphasechargeconservation0 = \frac{\partial}{\partial_x}\left(\sigma_s^{eff}\frac{\partial \phi_s}{\partial x}\right) - j^{Li} - a_{dl}C\frac{\partial(\phi_s - \phi_e)}{\partial x} \tag{10}$$

$$\text{Electrolyte charge conservation} 0 = \frac{\partial}{\partial_x}\left(k^{eff}\frac{\partial \phi_e}{\partial x}\right) + \frac{\partial}{\partial_x}\left(k_D^{eff}\frac{\partial \ln c_e}{\partial x}\right) + j^{Li} + a_{dl}C\frac{\partial(\phi_s - \phi_e)}{\partial x} \tag{11}$$

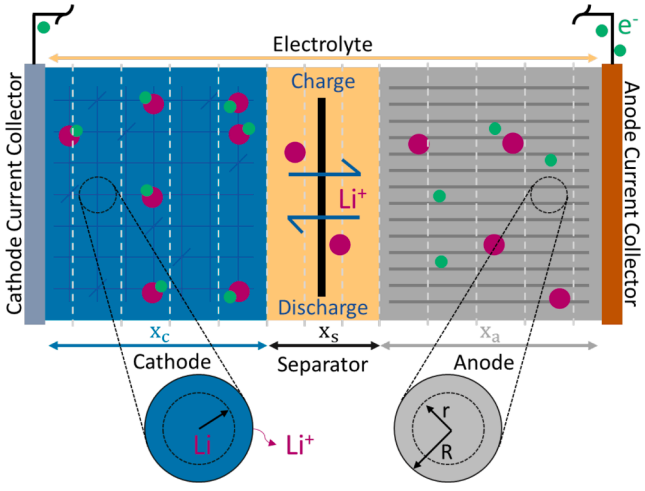

Fig. 5. Conceptual sketch of the pseudo-two-dimensional electrochemical model.

$$\rho c_p \frac{dT}{dt} = \dot{q}_{rxn} + \dot{q}_{rev} + \dot{q}_{ohm} + \dot{q}_c + \dot{q}_{conv} \text{ Thermal balance} \quad (12)$$

In addition to the described electrochemical model, the software also includes a series of degradation mechanisms such as solid electrolyte interface growth, lithium plating or material cracking, as well as mechano-electrochemical interaction through an active material swelling model. Since the number of additional models for degradation of the cell can be overwhelming and difficult to calibrate and discern, the initial battery characterization was performed without aging and degradation mechanisms. For the aging process, since only high temperature conditions (20 °C and 50 °C) are considered, the dominant mechanisms were simplified to only SEI growth. Other mechanisms like lithium plating are more relevant in conditions with problems for lithium allocation, like low temperature operation or very high current demands. To model this effect, two additional equations are considered. These equations will add a lithium loss term affecting the total capacity, as well as an increase in the internal resistance. First, the side reaction current density is obtained with a Tafel-like expression (Eq. (13)) to determine how much lithium is being consumed in this reaction. With this lithium consumption then a SEI growth rate is defined by Eq. (14) through the SEI layer thickness evolution. Lastly, the total resistance of the SEI is recalculated considering it thickness and its effective conductivity with Eq. Eqn 15 [46,47].

$$\text{SEI growth side reaction current } i_{SEI} = -i_{0,SEI}\exp\left(-\frac{a_{c,SEI}F}{RT}\left(\phi_s - \phi_e - U_{SEI} - \frac{j^{Li}}{a_s}R_{SEI}\right)\right) \quad (13)$$

$$\text{SEI thickness growth } \frac{\partial \delta_{SEI}}{\partial t} = -\frac{i_{SEI}}{2F}\frac{M_{SEI}}{\rho_{SEI}} \quad (14)$$

$$SEI associated resistance R_{SEI} = \frac{\delta_{SEI}}{k^{eff}_{SEI}} \quad (15)$$

2.4.3. Model calibration procedure

To characterize the batteries used in this study in order to obtain information about internal parameters of the cell, a calibration process was carried out using the Genetic Algorithm Optimizer included in the GT software. In a first step, the normal operation of the cell was calibrated using the voltage and temperature data from the constant-current tests of the cells in pristine conditions. For this optimization both, constructive parameters and electrochemical properties were optimized to match the performance of the cell. The data from transient evaluations was used as validation of the good performance of the model. Some results can be observed in Fig. 6 and more information about the calibration methodology can be found in the work from Garcia et al. [48,49]. In this first stage, these 14 parameters were optimized:

- Particle size at the anode and the cathode (μm)
- Layer thickness of anode, cathode and separator (μm)
- Anode and cathode total capacity (Ah)
- First charge and first discharge capacity of anode and cathode (mAh/g)
- Contact resistance of the cell (Φ/m^2)
- Specific heat capacity of the whole cell (J/kg K)
- Convective heat transfer coefficient (W/m^2 K)

A second calibration step was applied to consider aging through the capacity loss, as depited in Fig. 7. The paramters from the SEI growth model are calibrated to fit the temperature evolution as well as the capacity fade curve over the tested cycles. During this second calibration step, the previous set of parameters was freezed and only the SEI density and porosity, as well as the activation energy of the SEI formation reaction, from the SEI growth model were optimized.

From the calibrated model different data will be collected and utilized for the subsequent analysis included in this study. Parameters such as active material concentrations evolution over the aging process or constructive data like electrodes layer thicknesses will be necessary and obtained from the model. Table 3 and Table 4 show the main parameters obtained from the GT-Autolion model used to feed the stepwise reaction model for the NMC and LFP pristine batteries.

3. Results and discussion

This section presents the result and discussion of the thermal abuse experimental tests carried out in an ARC, with pristine and aged batteries. The main parameters are discussed in terms of the temperature, temperature rise rate and heat release behaviors. In addition, the mass before and after the destructive test is measured and used to support the results obtained. Stepwise reactions are approached to characterize the main heat release routes inside the battery. The results are used to discuss and support the aged effect on the battery thermal runaway process.

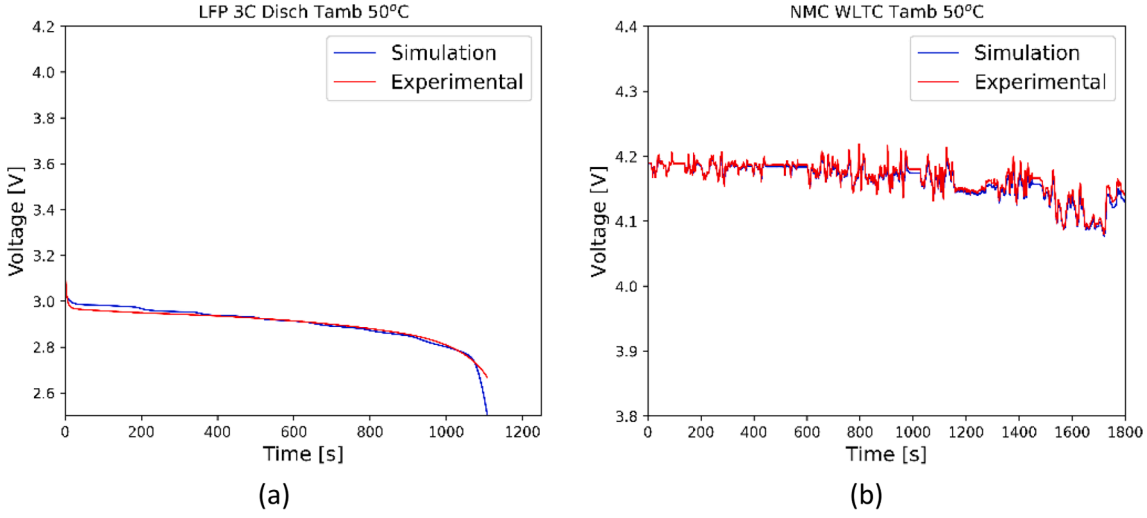

Fig. 6. Partial results of the model calibration including a calibrated curve at 3C for the LFP cell (a) and validation transient profile of the NMC cell (b).

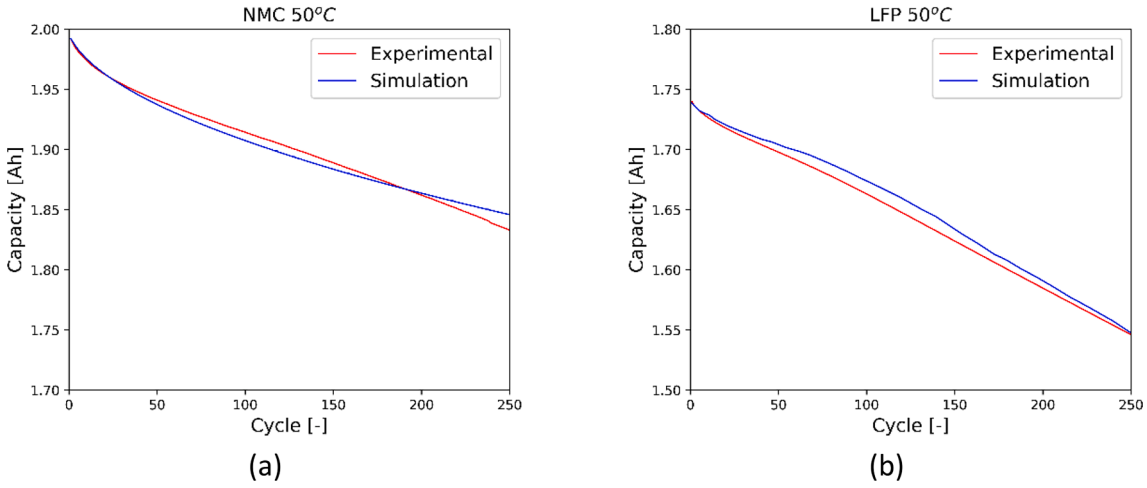

Fig. 7. Results of the aging model calibration for NMC cell (a) and LFP cell (b).

Table 3
Parameters from the P2D model used in the stepwise reactions for the NMC pristine battery.

		Anode	Cathode	Separator	Electrolyte
Thickness	micro m	89.118	92.140	34.310	–
Active Material Mass	g	6.822	12.798	–	–
Binder Mass	g	0.218	0.409	–	–
Conductive Agen Mass	g	0.218	0.409	–	–
Active Material Volume	mL	3.046	2.666	–	–
Binder Volume	mL	0.123	0.231	–	–
Conductive Agen Volume	mL	0.112	0.210	–	–
Total Mass	g	7.257	13.615	1.089	8.721
Total Volume	mL	3.280	3.107	1.513	7.268
Coated Volume	mL	4.908	4.803	1.513	
Density	g/cm3	2.212	4.383	1.200	1.2
Porosity	Fraction	0.332	0.353	0.400	–
Electrolyte volume	mL	3.004	3.106	1.157	
Electrolyte Coated moles	mol	0.036	0.037	0.014	
SEI Lithium	mol	1.45E-04			
Electrode Capacity	mAh/g	371.933	275.509	–	–
Stoichiometry at 100% SoC	–	0.884	0.322	–	–
Stoichiometry at 0% SoC	–	0.006	0.921	–	–
Active Material moles	mol	0.094671	0.131560444		0.087211
Lithium moles (@100% SoC)	mol	0.088844	0.044972316	–	–

Table 4
Parameters from the P2D model used in the stepwise reactions for the LFP pristine battery.

		Anode	**Cathode**	**Separator**	**Electrolyte**
Thickness	micro m	65.805	99.477	43.144	–
Active Material Mass	g	5.452	11.914	–	–
Binder Mass	g	0.174	0.380	–	–
Conductive Agen Mass	g	0.174	0.380	–	–
Active Material Volume	mL	2.434	3.310	–	–
Binder Volume	mL	0.098	0.215	–	–
Conductive Agen Volume	mL	0.089	0.195	–	–
Total Mass	g	5.800	12.675	1.757	8.111
Total Volume	mL	2.621	3.719	2.440	6.759
Coated Volume	mL	3.616	5.173	2.440	
Density	g/cm3	2.213	3.408	1.200	1.2
Porosity	Fraction	0.275	0.281	0.400	–
Electrolyte volume	mL	2.134	3.226	1.399	
Electrolyte Coated moles	mol	0.026	0.039	0.017	
SEI Lithium	mol	0.001			
Electrode Capacity	mAh/g	371.933	169.897	–	–
Stoichiometry at 100% SoC	–	0.898	0.033	–	–
Stoichiometry at 0% SoC	–	0.004	0.881	–	–
Active Material moles	mol	0.075652	0.075525353		0.081106
Lithium moles (@100% SoC)	mol	0.072121	0.002645839	–	

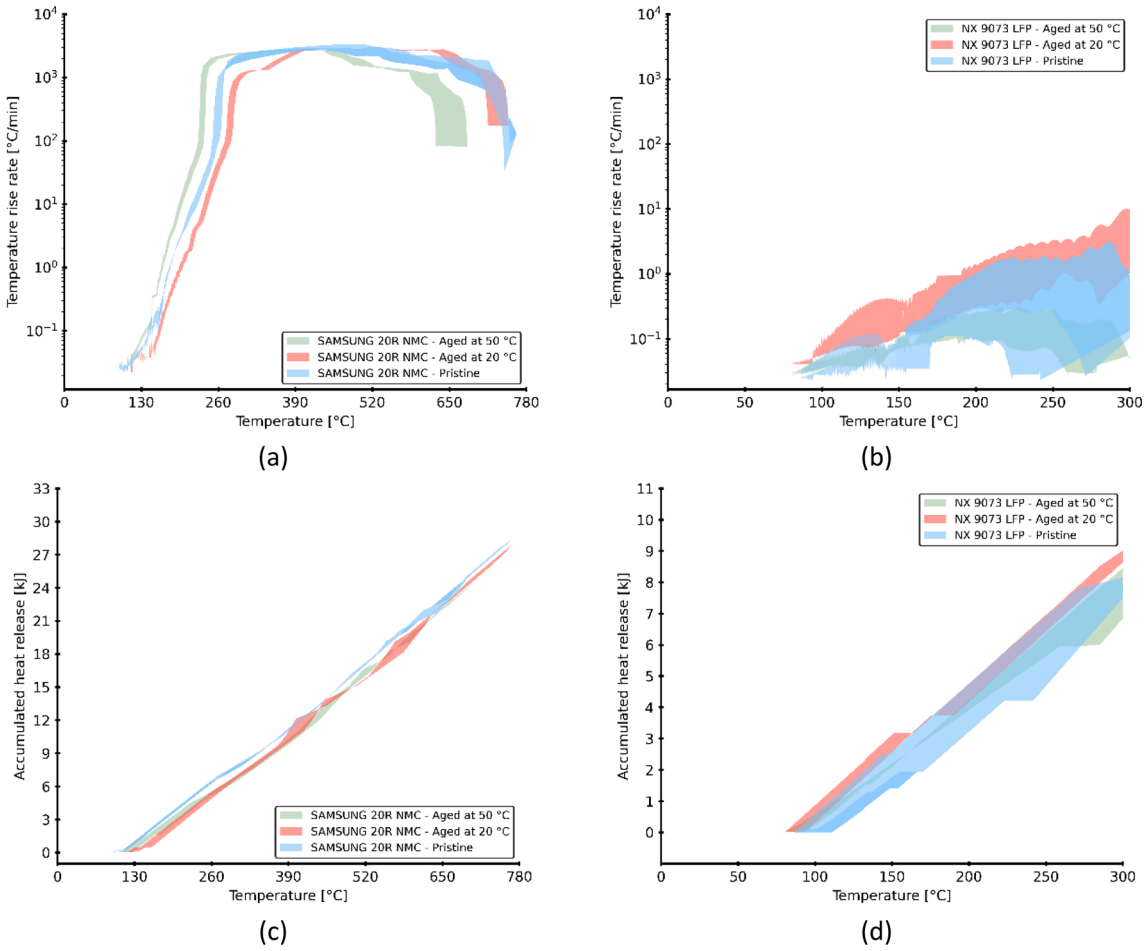

Fig. 8. Temperature rise rate and heat release as a function of temperature for pristine and aged batteries: (a) Temperature rise rate – NMC, (b) Temperature rise rate – LFP, (c) Heat released – NMC and (d) Heat released - LFP.

3.1. Thermal runaway test at constant pressure

Fig. 8 shows the temperature rise rate and accumulated heat release as a function of the battery temperature for pristine and aged batteries (NMC and LFP). The thermal runaway was induced through heating, using the heat-wait-seek protocol in an ARC. Fig. 8 (a) and Fig. 8 (c) present the results obtained for the NMC batteries. The NMC aged batteries at 50 °C of ambient temperature showed a higher temperature rise rate at the beginning of the process. In sequence, all batteries presented a similar maximum temperature rise rate and remained during a time. However, the chemical reactions slowed down, decreasing the temperature rise rate first for the NMC aged batteries at 50 °C of ambient temperature, then for the batteries aged at 20 °C ambient temperature, and lastly for the pristine batteries. Therefore, the aged battery at a higher ambient temperature would be more aggressive in the first stage of the thermal runaway process. Nevertheless, as depicted in Fig. 8 (c), the accumulated heat release showed higher values for the pristine batteries as its temperature rise rate remained higher during more time.

Fig. 8 (b) shows the temperature rise rate as a function of battery temperature for the pristine and aged LFP batteries. Using the same methodology applied to the NMC batteries, pristine LFP batteries were heated using the heat-wait-seek protocols until exothermic reactions began. In addition, the aged LFP batteries at 20 and 50 °C of ambient temperatures were also heated up to thermal runaway using the same protocols. Unlike the NMC batteries, the exothermic reactions that started to occur in the LFP batteries were not enough to self-sustain for all the batteries tested. Therefore, the aging effect on LFP batteries was insufficient to induce the thermal runaway. The blue area representing the values obtained from the pristine batteries coincides with the curves from the aged batteries. The same happened with the accumulated heat release depicted in Fig. 8 (d), which presents low values due to the

Table 5
Average maximum temperature, crucial temperature, onset temperature, maximum accumulated heat released and maximum temperature rise rate for pristine NMC and LFP batteries.

	SAMSUNG 20R NMC	NMC Average relative Difference (%)	NX 9073 LFP	LFP Average relative Difference [%]
Maximum temperature [°C]	753	0.9	280	9.3
Onset temperature [°C] (at 10 °C/min)	216	2.7	–	–
Crucial temperature [°C] (at 100 °C/min)	247.3	7.6	–	–
Maximum accumulated heat release [kJ]	28	1.0	5.5	25.3
Maximum temperature rise rate [°C/min]	3100	7.3	1.1	109.8
Initial mass (g)	42.8	0.3	40.0	1.5
End mass (g)	32.0	1.0	36.1	1.8
Mass difference (g)	10.8	2.5	3.9	9.0

abovementioned behavior.

Table 5 shows parameters related to the thermal runaway process for the NMC and LFP pristine batteries, respectively. LFP batteries did not exhibit a sufficient self-sustaining chemical reaction to induce thermal runaway during the heating tests. For this reason, the onset temperature and crucial temperature have no values. The maximum temperature was lower than 315 °C, presenting lower values of temperature rise rate and accumulated heat release. The temperature of 315 °C is the maximum temperature that the calorimeter can heat up. Thus, despite the small exothermic reactions during the external heating approach to trigger thermal runaway, it was not self-sustaining to induce the uncontrolled process. Unlike LFP pristine batteries, NMC pristine batteries showed enough self-sustaining exothermic reactions leading to thermal runaway. The maximum temperature achieved on average was about 753 °C, being the minimum onset and crucial temperatures about 216 and 247 °C, respectively. In addition, the onset temperature presented a lower average relative difference (2.7 %) than crucial temperature (7.6%) among the NMC pristine batteries, representing a parameter more constant for thermal runaway prediction. Moreover, the maximum accumulated heat released and temperature rise rate on average were 28 kJ and 3100 °C/min, respectively. These values are significantly higher than those obtained for LFP batteries, exemplifying the potential for thermal runaway. Furthermore, the mass loss for the NMC battery was greater than for the LFP battery, being the difference of about 10.8 g and 3.9 g, respectively. The LFP chemistry showed more significant variability in mass loss, which is reflected in the parameters shown in Fig. 8.

Table 6 and Table 7 depicts the thermal runaway parameters related to the aged batteries at 20 and 50 °C ambient temperatures for both NMC and LFP batteries, respectively. Aged LFP batteries showed no different effect when induced to thermal runaway. Thus, the results are similar to those described for pristine LFP batteries. Nevertheless, NMC aged batteries showed different results, especially for NMC aged battery at 50 °C. The average maximum temperature and temperature rise rate achieved were lower than the pristine NMC batteries. In addition, the thermal runaway process was triggered before, as illustrated by the lower onset temperature and crucial temperature. Comparing the mass losses, the results for the LFP batteries are similar to those from pristine conditions. NMC chemistry has shown higher losses for the aged condition with 50 °C ambient temperature, while the aged at 20 °C presented a value comparable with the pristine condition.

Table 6
Average thermodynamic properties for the NMC batteries aged at different ambient temperatures.

	SAMSUNG 20R NMC			
	Aged at 20 °C	NMC Average relative Difference (%)	Aged at 50 °C	NMC Average relative Difference (%)
Maximum temperature [°C]	740	1.5	660.2	2
Onset temperature [°C] (at 10 °C/min)	230.2	3	195.5	3.5
Crucial temperature [°C] (at 100 °C/min)	263.2	8	226.1	7.5
Maximum accumulated heat release [kJ]	25.5	1.1	24.2	1.0
Maximum temperature rise rate [°C/min]	2806.5	7.2	2806.5	7.4
Initial mass (g)	42.5	0.5	42.4	0.3
End mass (g)	32.6	1.1	30.2	1.0
Mass difference (g)	9.9	3.0	12.2	2.5

Table 7
Average thermodynamic properties for the LFP batteries aged at different ambient temperatures.

	NX 9073 LFP			
	Aged at 20 °C	LFP Average relative Difference [%]	Aged at 50 °C	LFP Average relative Difference [%]
Maximum temperature [°C]	314.7	2.0	315.0	1.0
Onset temperature [°C] (at 10 °C/min)	–	–	–	–
Crucial temperature [°C] (at 100 °C/min)	–	–	–	–
Maximum accumulated heat release [kJ]	9.2	15.2	8.2	30.4
Maximum temperature rise rate [°C/min]	4.6	50.3	0.2	80.1
Initial mass (g)	40.8	1.2	40.9	1.3
End mass (g)	36.6	2.0	36.7	1.2
Mass difference (g)	4.2	9.0	4.2	9.2

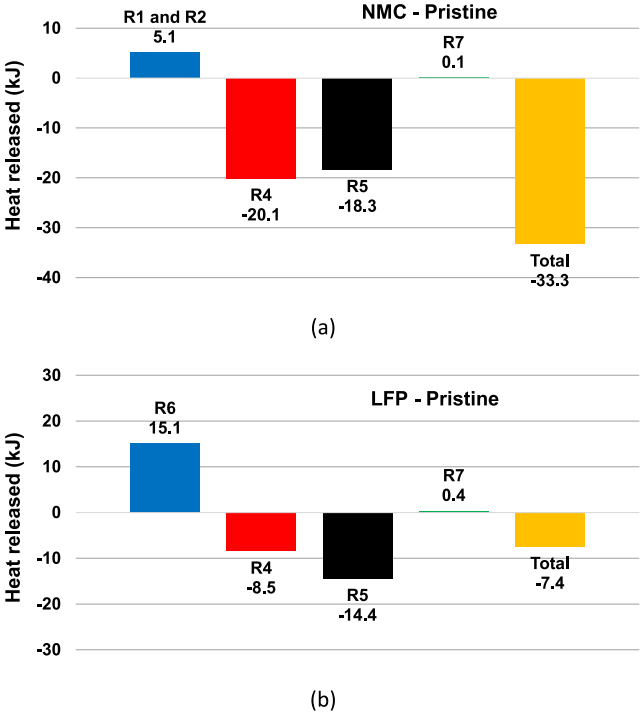

Fig. 9. Total heat release and as a function of each stepwise reaction for pristine NMC (a) and LFP (b) batteries.

3.2. Stepwise reactions analysis

Fig. 9 shows the total heat release and, separately, for each stepwise reaction related to cathode decomposition, electrolyte oxidation, SEI decomposition and anode-electrolyte reaction for the pristine NMC, Fig. 9 (a), and pristine LFP, Fig. 9 (b). The value obtained for the NMC pristine battery was similar to that obtained experimentally, considering both calculation forms. Reaction (4) and Reaction (5) seem to have the higher impact on the total heat release for the NMC battery. The last one is related to the SEI decomposition, which puts in direct contact the lithium and electrolyte. Compared with the LFP battery, the value resulting from Reaction (5) is of the same order as the NMC value. Both

reactions are expected to occur in both battery chemistries since the anode and electrolyte components are virtually the same. The more significant difference between the chemistry is related to the cathode decomposition reaction. For the LFP, the higher energy required to decompose the delithiated form in the cathode decreases the total energy released. The difference is about 10 kJ higher for the LFP battery. In addition, the oxygen released during this reaction is lower than the NMC battery. It resulted in a lower heat released in Reaction (4), a difference of about 11.5 kJ higher for the NMC chemistry.

Fig. 10 depicts the results of heat released for the aged NMC and LFP batteries at 50 °C. Due to the test characteristics carried out, the model created in the GT-Autolion considers only the SEI growth as the mechanism of capacity fading during battery cycling. The main outcome of this process is the reduction of the cycled lithium and the electrolyte present in the anode. The SEI growth increases the thickness using both elements, reducing the battery's capacity. Considering this process, the only influence that can occur in the heat release calculator is in Reaction (5) and Reaction (7). Both elements are directly in contact during Reaction (5), and less quantity results in less heat release. Compared with the Pristine case, Fig. 9, the heat released is lower, 12.3% for the NMC and 68.9% for the LFP. The higher heat release reduction for the LFP case is linked to the lower value already presented for this cathode chemistry.

Fig. 11 presents the heat released for the batteries LFP and NMC aged at 20 °C. For this temperature, the main mechanism for battery aging is also the SEI growth. However, the capacity fading was lower for both battery chemistries when compared to the result obtained at 50 °C. The SEI growth is reduced, resulting in more mols of lithium and electrolyte in the anode. For this reason, Reaction (5) has shown a higher value for the LFP and NMC batteries compared to results in Fig. 10, where the batteries were cycled at 50 °C. However, the values obtained were similar to the pristine batteries, Fig. 9. Compared with the experimental tests performed in Fig. 8 and Table 7, the results are in accordance as the values of heat release for the batteries aged at 20 °C were higher than those at 50 °C and similar to those presented for the pristine batteries.

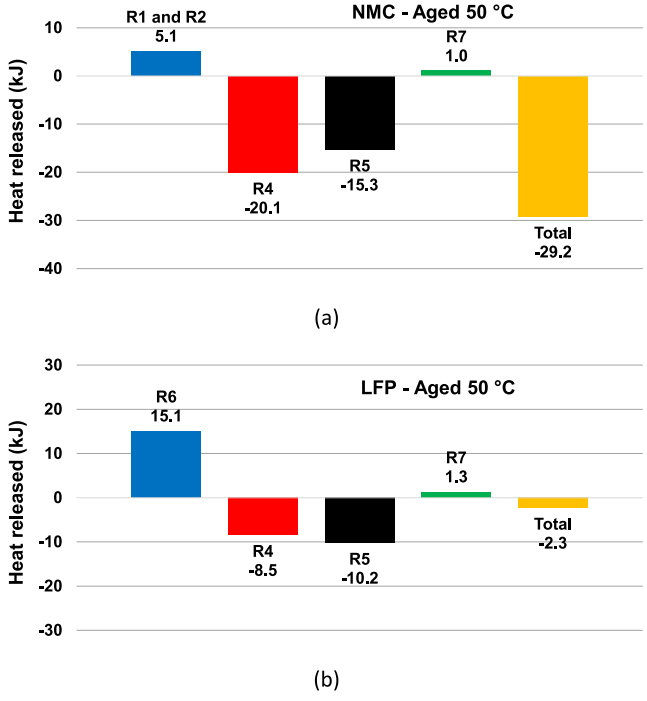

Fig. 10. Total heat release and as a function of each stepwise reaction for aged NMC (a) and LFP (b) batteries at 50 °C.

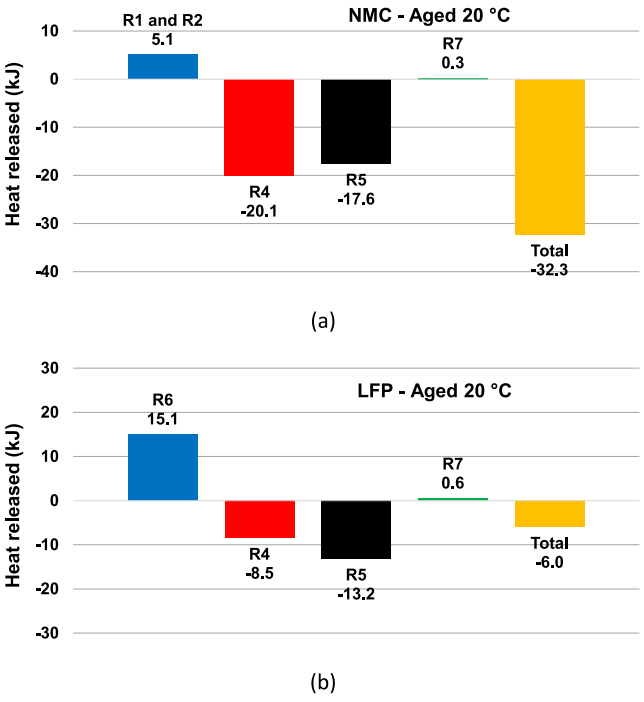

Fig. 11. Total heat release and as a function of each stepwise reaction for aged NMC (a) and LFP (b) batteries at 20 °C.

4. Conclusions

The present work showed an experimental investigation of the aging effect on the thermal runaway for two different cathode chemistry, NMC and LFP. An ARC was coupled with an Arbin bidirectional source and used to cycle the batteries up to 250 cycles in two different ambient temperatures, 20 °C and 50 °C. The aged batteries were subjected to external heating abuse using the ARC to evaluate the thermal runaway thermodynamic parameters. The heat-wait-seek protocol was used for the external heating test to trigger the thermal runaway. Pristine batteries with the same cathode chemistry were also induced thermal runaway to compare with the aged batteries. A computational model was created in the GT-Autolion software and calibrated with the data obtained from the experimental test. Parameters difficult to measure in the batteries were obtained from the GT-Autolion model and used in the heat release calculator. This table is based on stepwise reactions, and the results were used for given insights into the thermal runaway process for the pristine and aged batteries. Based on that, the following conclusion could be drawn:

- Experimental tests of thermal runaway abuse have shown that the pristine NMC battery release about 28 kJ against a maximum of 5.5 kJ from the LFP battery.
- Aged batteries at high temperatures showed lower heat released during thermal abuse with external heating as a thermal runaway trigger.
- The LFP batteries presented a great variability among the experimental test results. Nevertheless, higher thermal safety is evident when compared with the NMC battery.
- The thermal safety of the LFP battery can be attributed to the endothermic reaction of the cathode decomposition and the less oxygen released during this process, resulting in less heat released when the oxygen reacts with the electrolyte.
- For both cathode chemistry, the reaction between the lithium and electrolyte in the anode resulted in comparable values, since similar components form both anode and electrolyte.

- The aged batteries have SEI growth as the main mechanism for capacity fading. For this reason, the lithium and electrolyte present in the anode are reduced, resulting in less heat released during the thermal runaway process.

Therefore, the present work has demonstrated the potential of coupling the pseudo-two-dimensional model, to predict the effect of aging, with step-wise reactions to predict heat release due to thermal runaway. Both fresh and aged obtained similar values when comparing experiments and modeling. Future works would be helpful in extending the current work with more experimental tests, including different aging processes and different lithium-ion batteries, increasing the robustness of the current modeling and covering aspects such as repeatability.

CRediT authorship contribution statement

José Vicente Pastor: Writing – review & editing. **Antonio García:** Conceptualization, Methodology. **Javier Monsalve-Serrano:** Validation, Investigation, Writing – review & editing. **Diego Golke:** Formal analysis, Writing – original draft.

Declaration of Competing Interest

The authors declare that they have no known competing financial interests or personal relationships that could have appeared to influence the work reported in this paper.

Data availability

The authors do not have permission to share data.

Acknowledgment

Operación financiada por la Unión Europea a través del Programa Operativo del Fondo Europeo de Desarrollo Regional (FEDER) de la Comunitat Valenciana 2014-2020 con el objetivo de promover el desarrollo tecnológico, la innovación y una investigación de calidad. Proyecto IDIFEDER/2021/53, Equipamiento Para El Estudio Del Fenómeno De Combustión No Controlada En Baterías De Vehículos Eléctricos, entidad beneficiaria Universitat Politècnica de València. The authors also acknowledge the Vicerrectorado de Investigación de la Universitat Politècnica de València for supporting this research through the CONVOCATORIA de AYUDAS A GRUPOS INVESTIGADORES ACTIVOS EN CAPTACIÓN DE FONDOS DEL PLAN ESTATAL (PAID-11-21). This research is part of the project TED2021-132220B-C21, funded by the MCIN/AEI/10.13039/501100011033 and the European Union "NextGenerationEU"/PRTR.

References

[1] A. García, J. Monsalve-Serrano, R.L. Sari, S. Martínez-Boggio, Thermal runaway evaluation and thermal performance enhancement of a lithium-ion battery coupling cooling system and battery sub-models, Appl. Therm. Eng. 202 (2022), 117884, https://doi.org/10.1016/j.applthermaleng.2021.117884.

[2] G. Zhao, X. Wang, M. Negnevitsky, C. Li, An up-to-date review on the design improvement and optimization of the liquid-cooling battery thermal management system for electric vehicles, Appl. Therm. Eng. 219 (2023), 119626, https://doi.org/10.1016/j.applthermaleng.2022.119626.

[3] A. Kumar Thakur, R. Sathyamurthy, R. Velraj, R. Saidur, A.K. Pandey, Z. Ma, et al., A state-of-the art review on advancing battery thermal management systems for fast-charging, Appl. Therm. Eng. 226 (2023), 120303, https://doi.org/10.1016/j.applthermaleng.2023.120303.

[4] J. Liu, Z. Wang, J. Bai, T. Gao, N. Mao, Heat generation and thermal runaway mechanisms induced by overcharging of aged lithium-ion battery, Appl. Therm. Eng. 212 (2022), 118565, https://doi.org/10.1016/j.applthermaleng.2022.118565.

[5] A. García, P. Zhao, J. Monsalve-Serrano, D. Villalta, S. Martinez-Boggio, Optical diagnostics of the venting spray and combustion behaviour during Li-ion battery thermal runaway induced by ramp heating, Appl. Therm. Eng. 218 (2023), 119308, https://doi.org/10.1016/j.applthermaleng.2022.119308.

[6] A. García, J. Monsalve-Serrano, R. Lago Sari, S. Martinez-Boggio, An optical investigation of thermal runway phenomenon under thermal abuse conditions, Energy Convers Manag 246 (2021), 114663, https://doi.org/10.1016/j.enconman.2021.114663.

[7] X. Feng, M. Ouyang, X. Liu, L. Lu, Y. Xia, X. He, Thermal runaway mechanism of lithium ion battery for electric vehicles: A review, Energy Storage Mater. 10 (2018) 246–267, https://doi.org/10.1016/j.ensm.2017.05.013.

[8] Q. Zhang, J. Niu, Z. Zhao, Q. Wang, Research on the effect of thermal runaway gas components and explosion limits of lithium-ion batteries under different charge states, J Energy Storage 45 (2022), 103759, https://doi.org/10.1016/j.est.2021.103759.

[9] A. García, J. Monsalve-Serrano, R. Lago Sari, R.Á. Fogué, Numerical analysis of kinetic mechanisms for battery thermal runaway prediction in lithium-ion batteries, Int. J. Engine Res. 23 (2022) 1691–1707, https://doi.org/10.1177/14680874211029902.

[10] B. Lei, W. Zhao, C. Ziebert, N. Uhlmann, M. Rohde, H. Seifert, Experimental Analysis of Thermal Runaway in 18650 Cylindrical Li-Ion Cells Using an Accelerating Rate Calorimeter, Batteries 3 (2017) 14, https://doi.org/10.3390/batteries3020014.

[11] M. Ghiji, S. Edmonds, K. Moinuddin, A Review of Experimental and Numerical Studies of Lithium Ion Battery Fires, Appl. Sci. 11 (2021) 1247, https://doi.org/10.3390/app11031247.

[12] T. Waldmann, M. Wohlfahrt-Mehrens, Effects of rest time after Li plating on safety behavior—ARC tests with commercial high-energy 18650 Li-ion cells, Electrochim. Acta 230 (2017) 454–460, https://doi.org/10.1016/j.electacta.2017.02.036.

[13] D. Ren, H. Hsu, R. Li, X. Feng, D. Guo, X. Han, et al., A comparative investigation of aging effects on thermal runaway behavior of lithium-ion batteries, ETransportation 2 (2019), 100034, https://doi.org/10.1016/j.etran.2019.100034.

[14] T. Waldmann, A. Iturrondobeitia, M. Kasper, N. Ghanbari, F. Aguesse, E. Bekaert, et al., Review—Post-Mortem Analysis of Aged Lithium-Ion Batteries: Disassembly Methodology and Physico-Chemical Analysis Techniques, J. Electrochem. Soc. 163 (2016) A2149–A2164, https://doi.org/10.1149/2.1211609jes.

[15] I. Esho, K. Shah, A. Jain, Measurements and modeling to determine the critical temperature for preventing thermal runaway in Li-ion cells, Appl. Therm. Eng. 145 (2018) 287–294, https://doi.org/10.1016/j.applthermaleng.2018.09.016.

[16] A.V. Shelke, J.E.H. Buston, J. Gill, D. Howard, K.C. Abbott, S.L. Goddard, et al., Characterizing and predicting 21700 NMC lithium-ion battery thermal runaway induced by nail penetration, Appl. Therm. Eng. 209 (2022), 118278, https://doi.org/10.1016/j.applthermaleng.2022.118278.

[17] W. Zhang, Z. Liang, X. Yin, G. Ling, Avoiding thermal runaway propagation of lithium-ion battery modules by using hybrid phase change material and liquid cooling, Appl. Therm. Eng. 184 (2021), 116380, https://doi.org/10.1016/j.applthermaleng.2020.116380.

[18] Y. Zhang, W. Mei, P. Qin, Q. Duan, Q. Wang, Numerical modeling on thermal runaway triggered by local overheating for lithium iron phosphate battery, Appl. Therm. Eng. 192 (2021), 116928, https://doi.org/10.1016/j.applthermaleng.2021.116928.

[19] Z. An, K. Shah, L. Jia, Y. Ma, Modeling and analysis of thermal runaway in Li-ion cell, Appl. Therm. Eng. (2019;160.), https://doi.org/10.1016/j.applthermaleng.2019.113960.

[20] P. Liu, Y. Li, B. Mao, M. Chen, Z. Huang, Q. Wang, Experimental study on thermal runaway and fire behaviors of large format lithium iron phosphate battery, Appl. Therm. Eng. 192 (2021), 116949, https://doi.org/10.1016/j.applthermaleng.2021.116949.

[21] H. Wang, H. Xu, Z. Zhao, Q. Wang, C. Jin, Y. Li, et al., An experimental analysis on thermal runaway and its propagation in Cell-to-Pack lithium-ion batteries, Appl. Therm. Eng. 211 (2022), 118418, https://doi.org/10.1016/j.applthermaleng.2022.118418.

[22] K. Li, C. Xu, H. Wang, C. Jin, X. Rui, S. Chen, et al., Investigation for the effect of side plates on thermal runaway propagation characteristics in battery modules, Appl. Therm. Eng. 201 (2022), 117774, https://doi.org/10.1016/j.applthermaleng.2021.117774.

[23] H. Zhang, C. Li, R. Zhang, Y. Lin, H. Fang, Thermal analysis of a 6s4p Lithium-ion battery pack cooled by cold plates based on a multi-domain modeling framework, Appl. Therm. Eng. 173 (2020), 115216, https://doi.org/10.1016/j.applthermaleng.2020.115216.

[24] P. Lyu, Y. Huo, Z. Qu, Z. Rao, Investigation on the thermal behavior of Ni-rich NMC lithium ion battery for energy storage, Appl. Therm. Eng. 166 (2020), 114749, https://doi.org/10.1016/j.applthermaleng.2019.114749.

[25] Z. Chen, Y. Qin, Z. Dong, J. Zheng, Y. Liu, Numerical study on the heat generation and thermal control of lithium-ion battery, Appl. Therm. Eng. 221 (2023), 119852, https://doi.org/10.1016/j.applthermaleng.2022.119852.

[26] A.M. Bates, Y. Preger, L. Torres-Castro, K.L. Harrison, S.J. Harris, J. Hewson, Are solid-state batteries safer than lithium-ion batteries? Joule 6 (2022) 742–755, https://doi.org/10.1016/j.joule.2022.02.007.

[27] R.C. Shurtz, J.D. Engerer, J.C. Hewson, Predicting High-Temperature Decomposition of Lithiated Graphite: Part II. Passivation Layer Evolution and the Role of Surface Area, J. Electrochem. Soc. 165 (2018) A3891–A3902, https://doi.org/10.1149/2.0171814jes.

[28] R.C. Shurtz, J.D. Engerer, J.C. Hewson, Predicting High-Temperature Decomposition of Lithiated Graphite: Part I. Review of Phenomena and a Comprehensive Model, J. Electrochem. Soc. 165 (2018) A3878–A3890, https://doi.org/10.1149/2.0541816jes.

[29] R.C. Shurtz, J.C. Hewson, Review—Materials Science Predictions of Thermal Runaway in Layered Metal-Oxide Cathodes: A Review of Thermodynamics,

J. Electrochem. Soc. 167 (2020), 090543, https://doi.org/10.1149/1945-7111/ab8fd9.
[30] High Precision Battery Test Equipment | Arbin Instruments n.d. https://arbin.com/ (accessed November 26, 2022).
[31] EV+ Accelerating Rate Calorimeter | Thermal Hazard Technology n.d. https://www.thermalhazardtechnology.com/battery-products/ev-plus-accelerating-rate-calorimeter (accessed November 26, 2022).
[32] D.I. Townsend, J.C. Tou, Thermal hazard evaluation by an accelerating rate calorimeter, Thermochim Acta 37 (1980) 1–30, https://doi.org/10.1016/0040-6031(80)85001-5.
[33] R.C. Shurtz, A Thermodynamic Reassessment of Lithium-Ion Battery Cathode Calorimetry, J. Electrochem. Soc. 167 (2020), 140544, https://doi.org/10.1149/1945-7111/abc7b4.
[34] K.W. Nam, W.S. Yoon, X.Q. Yang, Structural changes and thermal stability of charged LiNi1/3Co1/3Mn1/3O2 cathode material for Li-ion batteries studied by time-resolved XRD, J. Power Sources 189 (2009) 515–518, https://doi.org/10.1016/j.jpowsour.2008.10.130.
[35] L. Wang, T. Maxisch, G. Ceder, A first-principles approach to studying the thermal stability of oxide cathode materials, Chem. Mater. 19 (2007) 543–552, https://doi.org/10.1021/cm0620943.
[36] S. Sharifi-Asl, J. Lu, K. Amine, R. Shahbazian-Yassar, Oxygen Release Degradation in Li-Ion Battery Cathode Materials: Mechanisms and Mitigating Approaches, Adv. Energy Mater. 9 (2019) 1900551, https://doi.org/10.1002/aenm.201900551.
[37] G. Chen, T.J. Richardson, Thermal instability of Olivine-type LiMnPO4 cathodes, J. Power Sources 195 (2010) 1221–1224, https://doi.org/10.1016/j.jpowsour.2009.08.046.
[38] A.W. Golubkov, S. Scheikl, R. Planteu, G. Voitic, H. Wiltsche, C. Stangl, et al., Thermal runaway of commercial 18650 Li-ion batteries with LFP and NCA cathodes - Impact of state of charge and overcharge, RSC Adv. 5 (2015) 57171–57186, https://doi.org/10.1039/c5ra05897j.
[39] P. Röder, N. Baba, K.A. Friedrich, H.D. Wiemhöfer, Impact of delithiated Li0FePO4 on the decomposition of LiPF6-based electrolyte studied by accelerating rate calorimetry, J. Power Sources 236 (2013) 151–157, https://doi.org/10.1016/j.jpowsour.2013.02.044.
[40] S.P. Ong, A. Jain, G. Hautier, B. Kang, G. Ceder, Thermal stabilities of delithiated olivine MPO4 (M = Fe, Mn) cathodes investigated using first principles calculations, Electrochem. Commun. 12 (2010) 427–430, https://doi.org/10.1016/j.elecom.2010.01.010.
[41] S. Zheng, L. Wang, X. Feng, X. He, Probing the heat sources during thermal runaway process by thermal analysis of different battery chemistries, J. Power Sources 378 (2018) 527–536, https://doi.org/10.1016/j.jpowsour.2017.12.050.
[42] A. Kvasha, C. Gutiérrez, U. Osa, I. de Meatza, J.A. Blazquez, H. Macicior, et al., A comparative study of thermal runaway of commercial lithium ion cells, Energy 159 (2018) 547–557, https://doi.org/10.1016/j.energy.2018.06.173.
[43] T. Gao, J. Bai, D. Ouyang, Z. Wang, W. Bai, N. Mao, et al., Effect of aging temperature on thermal stability of lithium-ion batteries: Part A – High-temperature aging, Renew. Energy 203 (2023) 592–600, https://doi.org/10.1016/j.renene.2022.12.092.
[44] Y. Xie, H.T. Yu, T.F. Yi, Y.R. Zhu, Understanding the thermal and mechanical stabilities of olivine-type LiMPO4 (M = Fe, Mn) as cathode materials for rechargeable lithium batteries from first principles, ACS Appl. Mater. Interfaces 6 (2014) 4033–4042, https://doi.org/10.1021/am4054833.
[45] Newman, John; Balsara NP. ELECTROCHEMICAL SYSTEMS. vol. 1. 4[a]. Hoboken, USA: John Wiley & Sons, Inc.; 2021.
[46] C.D. Rahn, C. Wang, Battery Systems Engineering, Wiley (2013), https://doi.org/10.1002/9781118517048.
[47] G. Technologies, AutoLion Application Manual and Calibration Procedure, Westmont, Illinois, 2021.
[48] A. García, J. Monsalve-Serrano, A. Ponce-Mora, Á. Fogué-Robles, Development of a calibration methodology for fitting the response of a lithium-ion cell P2D model using real driving cycles, Energy (2023;271.), https://doi.org/10.1016/j.energy.2023.126992.
[49] A. García, J. Monsalve-Serrano, S. Martinez-Boggio, D. Golke, Energy assessment of the ageing phenomenon in Li-Ion batteries and its impact on the vehicle range efficiency, Energy Convers. Manag. 276 (2023), 116530, https://doi.org/10.1016/j.enconman.2022.116530.